NANO MICRO small
www.small-journal.com

Porous Carbon-Hosted Atomically Dispersed Iron–Nitrogen Moiety as Enhanced Electrocatalysts for Oxygen Reduction Reaction in a Wide Range of pH

Shaofang Fu, Chengzhou Zhu, Dong Su, Junhua Song, Siyu Yao, Shuo Feng, Mark H. Engelhard, Dan Du, and Yuehe Lin**

As one of the alternatives to replace precious metal catalysts, transition-metal–nitrogen–carbon (M–N–C) electrocatalysts have attracted great research interest due to their low cost and good catalytic activities. Despite nanostructured M–N–C catalysts can achieve good electrochemical performances, they are vulnerable to aggregation and insufficient catalytic sites upon continuous catalytic reaction. In this work, metal–organic frameworks derived porous single-atom electrocatalysts (SAEs) were successfully prepared by simple pyrolysis procedure without any further posttreatment. Combining the X-ray absorption near-edge spectroscopy and electrochemical measurements, the SAEs have been identified with superior oxygen reduction reaction (ORR) activity and stability compared with Pt/C catalysts in alkaline condition. More impressively, the SAEs also show excellent ORR electrocatalytic performance in both acid and neutral media. This study of nonprecious catalysts provides new insights on nanoengineering catalytically active sites and porous structures for nonprecious metal ORR catalysis in a wide range of pH.

Oxygen reduction reaction (ORR) plays a crucial role in energy conversion and storage devices, such as fuel cells and metal–air batteries.[1–5] Nowadays, Pt nanoparticles loaded on carbon supports (Pt/C) with the high surface area are considered as the state-of-the-art electrocatalysts for ORR. Whereas, some issues of Pt/C catalysts need to be resolved before the widespread implementation of these devices, including Pt dissolution, catalysts poisoning, and poor methanol tolerance.[6–8] In addition, the high price and scarcity of Pt also hinder their further commercialization. To address these issues, nonprecious metal nanocatalysts (NPMNs), obtained from earth-abundant elements (Fe, N, C, Co, S, and so on), have attracted increasing attention and been studied extensively.[9–12] Among them, Fe-based carbonaceous catalysts, with Fe–N–C active sites, are the most promising NPMNs for ORR.[13–15] Their activity and stability in alkaline media can approach or even outperform those of Pt/C.[16,17] This has stimulated researchers to develop efficient catalysts with a high density of Fe–N–C active sites through the rational design of their nanostructures. On the other hand, rapidly emerging studies on single-atom catalysts featured with homogeneity of the catalytic active site, low-coordination environment of the metal atom as well as the maximum metal utilization efficiency have received great consideration because of their high electrocatalytic properties.[18–21] Constructing Fe–N–C structures with single-atom feature is considered as the most efficient strategy, which allows the even dispersion of highly active Fe–N–C active sites and ensures the high ORR performance.[15,19,22–25] For instance, our group reported a facile and universal strategy to synthesize Fe,N-doped carbon nanotube aerogels with single-atom feature, which exhibited excellent electrocatalytic activity and durability for ORR in alkaline condition.[15] Besides, atomically FeN_2 moieties-modified mesoporous carbon,[24] N-doped porous carbon,[25] and cubic carbon frameworks[26] with atomically dispersed active sites were reported previously with highly efficient ORR performance in alkaline conditions.

Precisely tuning the morphology of the electrocatalysts to realize large surface area and pore volume is considered as another efficient approach for improving their performances. The porous structures can not only provide more exposed active sites but facilitate mass-transport for electrocatalytic reactions. As typical porous materials, metal–organic frameworks (MOFs), which are composed of well-organized metal centers

Dr. S. Fu, Dr. C. Zhu, J. Song, S. Feng, Dr. D. Du, Prof. Y. Lin
School of Mechanical and Materials Engineering
Washington State University
WA 99164, USA
E-mail: zhuchzh@gmail.com; yuehe.lin@wsu.edu
Dr. C. Zhu, Dr. D. Du
Key Laboratory of Pesticide and Chemical Biology
Ministry of Education, College of Chemistry
Central China Normal University
Wuhan 430079, P. R. China
Dr. D. Su
Center for Functional Nanomaterials
Brookhaven National Laboratory
Upton, NY 11973, USA
Dr. S. Yao
Chemistry Department
Brookhaven National Laboratory
Upton, NY 11973, USA
M. H. Engelhard
Environmental Molecular Science Laboratory
Pacific Northwest National Laboratory
Richland, WA 99354, USA
The ORCID identification number(s) for the author(s) of this article can be found under https://doi.org/10.1002/smll.201703118.

DOI: 10.1002/smll.201703118

and organic ligands, are promising templates or precursors for porous nanomaterials in energy applications, including fuel cells, supercapacitors, and batteries.[27–32] In addition to the large surface area, the composition of the resultant M–N–C catalysts can be easily controlled by substituting the metals or linkers. More recently, MOF-derived M–N–C porous materials have been proven to possess comparable or even better ORR catalytic activity compared with commercial Pt/C.[12,33,34] In comparison with the traditional raw materials, MOFs are ideal precursors, which contain metal, nitrogen, and carbon precursors in one single framework.[12] Herein, we developed an efficient strategy to synthesize highly efficient ORR electrocatalysts featured by single active sites and high surface area through simple pyrolysis of MOF precursors. Importantly, these MOF-derived single-atom electrocatalysts (SAEs) display excellent ORR catalytic performance in alkaline, acid, and neutral media, which is attributed to the highly exposed homogeneous active sites and morphological advantages. This facile procedure paves a new way for the preparation of SAEs for ORR in a wide range of pH.

The preparation of Fe-doped MOF precursors, zeolitic imidazolate frameworks, was similar to the previous report except for the addition of a certain amount of $Fe(NO_3)_3$ as shown in **Figure 1**A.[35] The details are available in the Experimental Section in the Supporting Information. After the pyrolysis of MOF precursors at different temperatures, a series of Fe_x–N–C–T (x = amount of Fe precursors, T = pyrolysis temperature) SAEs were obtained. Figure 1B shows the typical transmission electron microscopy (TEM) images of Fe_{50}–N–C-900 SAEs. It indicates that the dodecahedral structure was well maintained after pyrolysis. The average size of Fe_{50}–N–C-900 SAEs is around 87 nm. The component of Fe_{50}–N–C-900 SAEs was identified by electron energy loss spectroscopy (EELS) and mapping. The EELS spectrum of Fe_{50}–N–C-900 SAEs in Figure 1D reveals that C, N, O, and Zn are the dominant species. From the mapping profile (Figure 1E), we can see that these elements are uniformly distributed throughout the nanostructure. It should be noted that Fe was hard to be detected because of the small amount. The presence of Zn in Fe_{50}–N–C-900 SAEs indicates that Zn was not completely evaporated during the pyrolysis process. The single-atom features of Fe_{50}–N–C-900 were then confirmed by high-angle annular dark-field scanning transmission electron microscope (HAADF-STEM). Figure 1F clearly shows some bright dots in HAADF-STEM image, ascribing to Zn and Fe atoms, due to the Z-contrast between metal and carbon. These isolated metal atoms confirm the single-atom feature of Fe_{50}–N–C-900 SAEs. To study the effect of Fe concentration and analysis temperature on the morphology, N–C-900 and other SAEs with different Fe were also prepared. The corresponding TEM images in Figure S1 (Supporting Information) suggest that the size of resultant catalysts increases with the increase of Fe content. Whereas, the annealing temperature does not have much effect on the morphology of Fe–N–C SAEs, as shown in Figure S2 (Supporting Information).

X-ray diffraction (XRD) was then carried out to study the crystalline structure of SAEs. **Figure 2**A shows that two broad

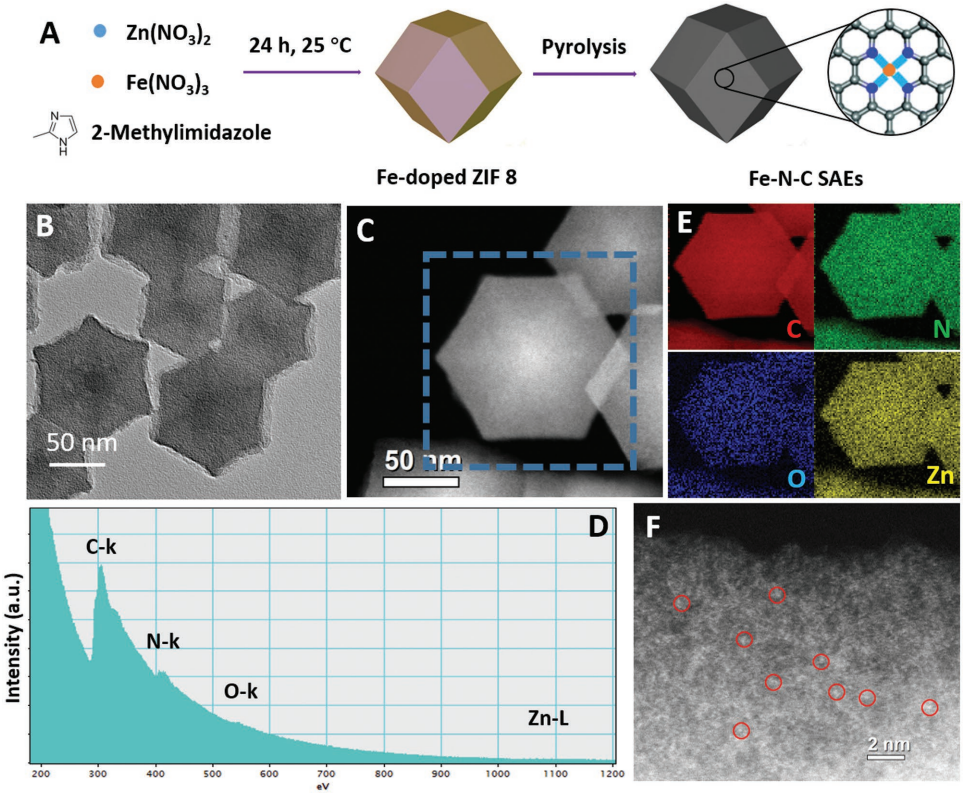

Figure 1. A) Schematic synthesis of MOF-derived Fe–N–C SAEs. B) TEM, C,F) HAADF-STEM images of Fe_{50}–N–C-900 SAEs. D) EELS spectrum of Fe_{50}–N–C-900 SAEs. E) Elemental distribution of C, N, O, and Zn in Fe_{50}–N–C-900 SAEs.

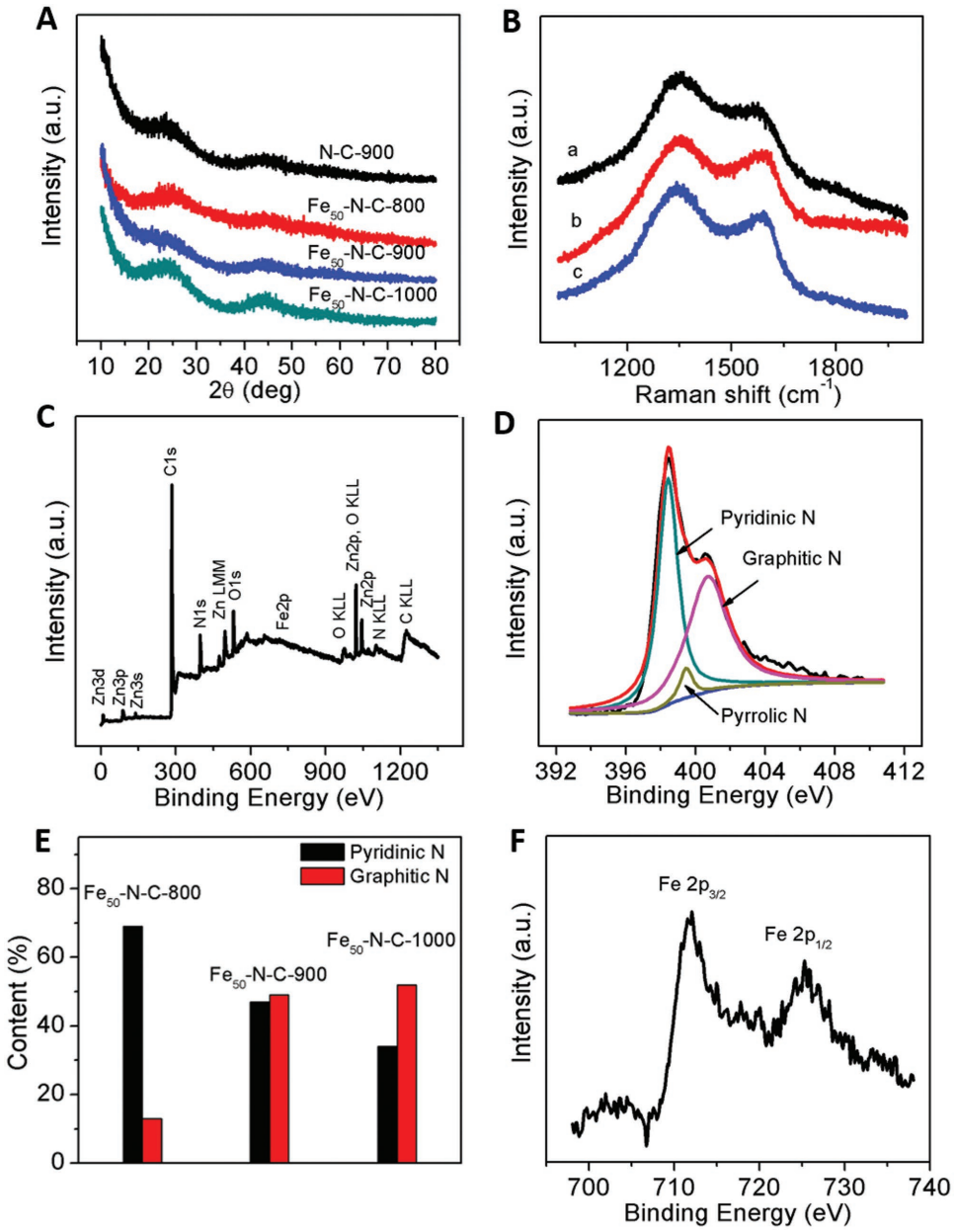

Figure 2. A) XRD patterns of various catalysts. B) Raman spectra of Fe_{50}–N–C SAEs with different temperatures (a: Fe_{50}–N–C-800. b: Fe_{50}–N–C-900. c: Fe_{50}–N–C-1000). C) XPS spectrum of Fe_{50}–N–C-900. D) High-resolution XPS spectrum of N in Fe_{50}–N–C-900. E) N content in Fe_{50}–N–C-900. F) High-resolution XPS spectrum of Fe in Fe_{50}–N–C-900.

peaks at around 24° and 44° were detected in N–C-900 and Fe_{50}–N–C SAEs, corresponding to the (002) and (100) planes of graphitic carbon. The Raman spectra of Fe_{50}–N–C SAEs with different pyrolysis temperature (Figure 2B) show two peaks at Raman shift of ≈1350 and 1590 cm^{-1}, indicating the D band and G band in graphite, respectively. All Fe_{50}–N–C SAEs show higher D band peak, indicating the large amount of high disordered carbon with abundant defects, which is beneficial for catalytic performance.[36–38] It should be noted that the content of C, O, N, Zn, and Fe in Fe_{50}–N–C-900 SAEs is 80.67, 7.54, 9.79, 1.85, and 0.15 at%, respectively. There is still a small amount of Zn maintained in the final products even under a much higher pyrolysis temperature (≈1.8 at% Zn in Fe_{50}–N–C-1000) as shown in Table S1 (Supporting Information). The information of surface composition and oxidation states was obtained by X-ray photoelectron spectroscopy (XPS) analysis as revealed in Figure 2C. The high-resolution N 1s XPS spectrum in Fe_{50}–N–C-900 (Figure 2D) was further deconvoluted into three peaks at 398.42, 399.45, and 400.69 eV, in correspondence with pyridinic N, pyrrolic N, and graphitic N.[39,40] Among them, pyridinic N and graphitic N are the dominant species with the atomic percentage of 47.36% and 48.65%, respectively.

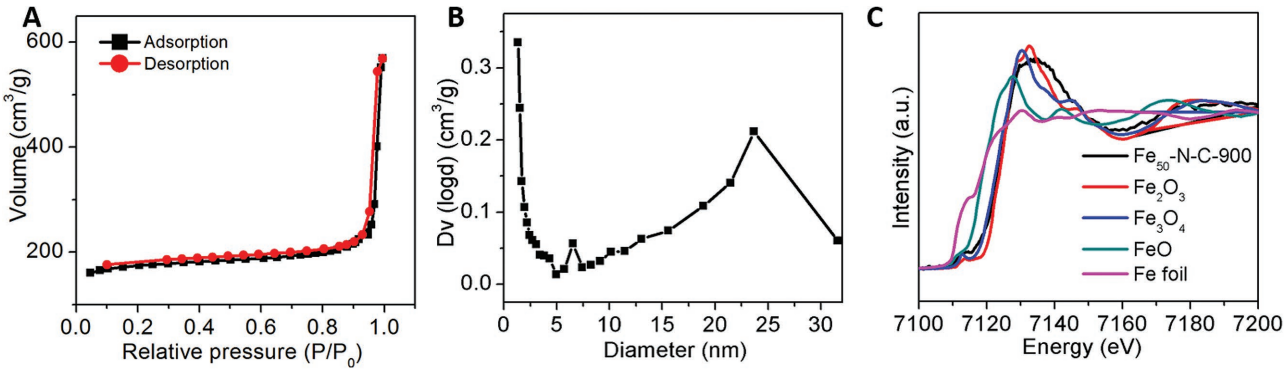

Figure 3. A) Nitrogen adsorption and desorption isotherms and B) pore size distribution curve of Fe_{50}–N–C-900. C) Fe K-edge XANES spectra of Fe_{50}–N–C-900 and reference samples.

In comparison with Fe_{50}–N–C-800 and Fe_{50}–N–C-1000, Fe_{50}–N–C SAEs exhibit the highest content of pyridinic N and graphitic N (Figure 2E). These two forms of N were demonstrated to be favorable for ORR.[15,41] Figure 2F shows the high-resolution XPS spectrum of Fe 2p in Fe_{50}–N–C SAEs. The two peaks at 711.8 and 725.4 eV indicate the presence of Fe (II) and Fe (III).

To get insight into the surface area and porosity property of the MOF-derived SAEs, N_2 adsorption/desorption profile of Fe_{50}–N–C-900 is revealed in **Figure 3**A,B. The Brunauer–Emmett–Teller surface area and pore volume is 540.3 m^2 g^{-1} and 0.88 cm^3 g^{-1}. The pore size distribution curve indicates that micro and mesopores are dominant in Fe_{50}–N–C-900. The high surface area and large pore volume can contribute faster mass-transport and electron-transfer process, resulting in improved ORR electrocatalysis.[2] To further confirm the structure of Fe_{50}–N–C-900 SAEs, X-ray absorption analysis was carried out. The X-ray absorption near-edge structure (XANES) in Figure 3C shows that the near-edge absorption energy of Fe_{50}–N–C-900 is between that of standard Fe foil and Fe_2O_3, indicating Fe atoms in the SAEs were positively charged, which was related to the N-coordination in single-atom catalysts."[22,39]

Upon the investigation of structural and compositional properties of Fe_{50}–N–C-900 SAEs, we next studied their ORR electrocatalytic performance in an alkaline solution using the rotating disk electrode (RDE). For comparison, the ORR catalytic activity of commercial Pt/C, N–C-900, and Fe–N–C with different synthesis condition was also investigated. **Figure 4**A shows the RDE polarization curves of C-N-900, Fe_{50}–N–C-900 SAEs, and Pt/C catalysts in 0.1 M KOH solution with a scan rate of 10 mV s^{-1} and a rotation rate of 1600 rpm. According to the linear sweep voltammetry (LSV) curves, Fe_{50}–N–C-900 SAEs possess the highest ORR activity with a more positive onset potential (1.00 V) and half-wave potential (0.92 V) compared with N–C-900 (0.87 and 0.81 V) and Pt/C (0.95 and 0.85 V). Importantly, the performance of Fe_{50}–N–C-900 also outperforms that of other Fe–N–C SAEs obtained under different synthesis condition and the ORR catalysts reported in others' works as shown in Figure S3 and Table S2 in the Supporting Information. To further confirm the structural and compositional advantages of Fe_{50}–N–C-900 SAEs, Tafel plots of Fe_{50}–N–C-900 SAEs and Pt/C were derived from Figure 4A. The Tafel slope (Figure 4B) of Fe_{50}–N–C-900 SAEs is 77 mV dec^{-1}, which is smaller than that of Pt/C (86 mV dec^{-1}). All these results, including much more positive onset potential and half-wave potential as well as small Tafel slope, suggest that the single active sites are extremely efficient for ORR. Figure 4C provides the RDE polarization curves at rotation rate ranging from 225 to 2500 rpm, which exhibit rotation rate-dependent current density. Based on these LSV curves, Koutecky–Levich (K–L) plots at various potential were obtained and revealed in Figure 3C inset. The good linearity and parallelism indicate the consistent electron-transfer number and first-order reaction kinetics regarding the oxygen concentration. Accordingly, the kinetic current densities (j_k) of Fe_{50}–N–C-900 and Pt/C at certain potentials were calculated. As illustrated in Figure 4D, Fe_{50}–N–C-900 catalysts possess much higher j_k than that of Pt/C. We next conducted the rotating ring-disk electrode (RRDE) tests to clarify the ORR pathway and HO_2^- yield. Based on the RRDE measurements, the average electron-transfer number on Fe_{50}–N–C-900 is 3.95, which is similar as that of Pt/C (3.97) as illustrated in Figure S3C (Supporting Information). In addition, the HO_2^- yield is less than 10% (Figure 4E), further confirming the four-electron ORR pathway on Fe_{50}–N–C-900 electrode. Aside from the activity, methanol tolerance is another important factor to evaluate the performance of ORR electrocatalysts in fuel cells. As expected, Fe_{50}–N–C-900 SAEs present much better tolerance to methanol than Pt/C, as shown in Figure S4 (Supporting Information). Remarkably, Fe_{50}–N–C-900 SAEs also possess exceptional long-term durability. In contrast with the substantial current drop-off of Pt/C electrode (Figure 4), Fe_{50}–N–C-900 exhibited a constant current during the stability test. Additionally, the robustness of the SAEs was further confirmed by the morphology study. No aggregation or collapse was observed in Fe_{50}–N–C-900 as revealed in Figure S5 (Supporting Information).

The exceptional ORR catalytic performance of Fe_{50}–N–C-900 SAEs in alkaline solution promoted us to study their activity in acid and neutral conditions. **Figure 5**A shows the RDE polarization curve of Fe_{50}–N–C-900, which possesses onset potential of 0.847 V and high limit current density of

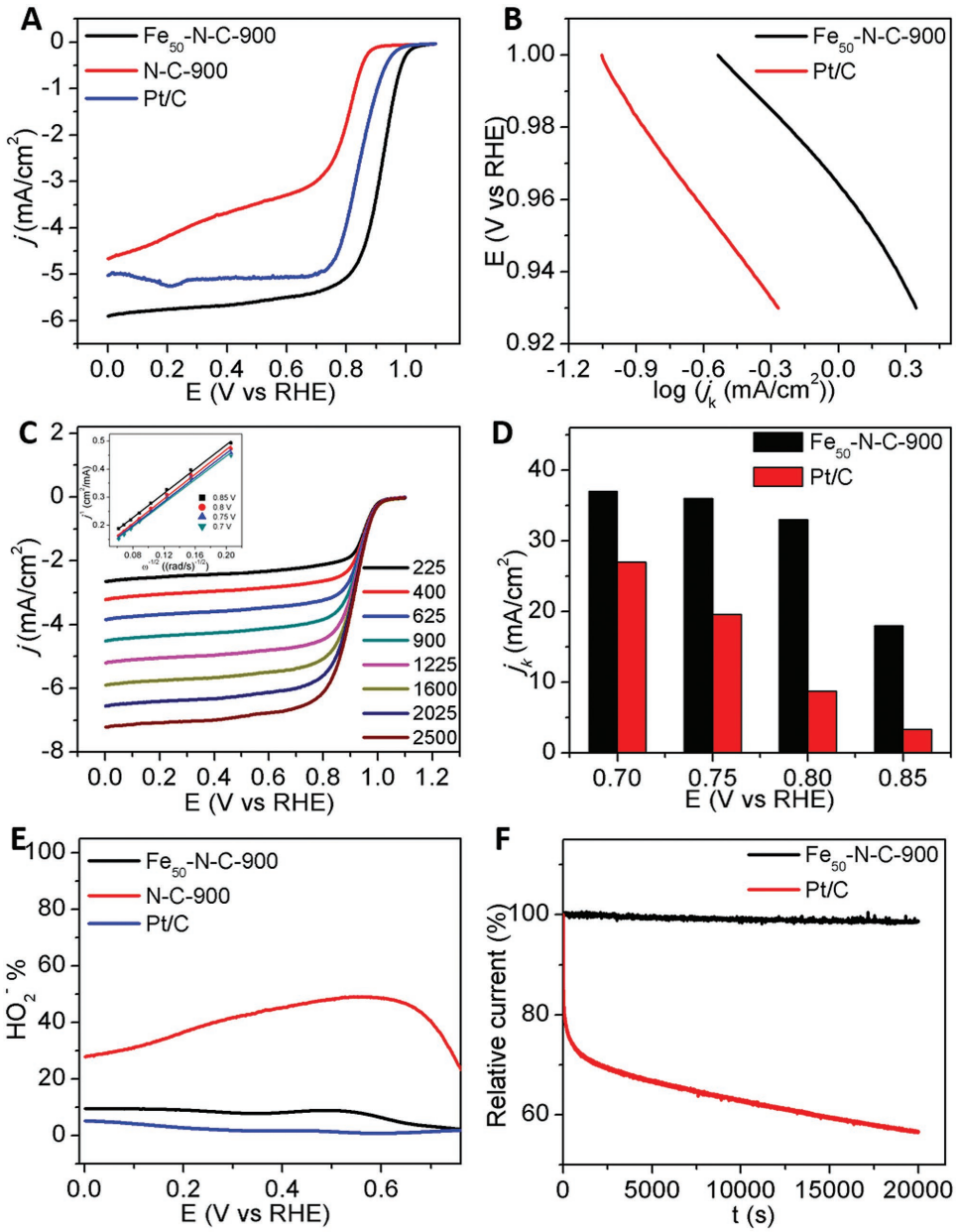

Figure 4. A) RDE polarization curves of Fe_{50}–N–C-900, N–C-900 and commercial Pt/C catalysts in O_2-saturated 0.1 M KOH solution at a scan rate of 10 mV s^{-1} and a rotation rate of 1600 rpm. B) Tafel plots of Fe_{50}–N–C-900 and Pt/C derived from Figure 3A. C) RDE polarization curves on Fe_{50}–N–C-900 at different rotation rates and corresponding K–L plots (inset). D) Kinetic current density (j_k) of the Fe_{50}–N–C-900 and Pt/C at different potentials. E) HO_2^- yield percentage on various catalysts derived from RRDE analysis. F) Current versus time (i–t) chronoamperometric response of the Fe_{50}–N–C-900 and Pt/C at 0.7 V in O_2-saturated 0.1 M KOH at 200 rpm, respectively. The loading is 0.1 mg cm^{-2} for all catalysts.

6.83 mA cm^{-2}. Based on the RRDE measurement results, the H_2O_2 yield on Fe_{50}–N–C-900 electrode is lower than 10% (Figure 5B), confirming the four-electron pathway. It is worth noting that more than 50% current density was retained on Fe_{50}–N–C-900 electrode after long-term stability test. Whereas, around 70% current loss was observed on Pt/C electrode, as shown in Figure 5C. Remarkably, Fe_{50}–N–C-900 SAEs reveal good ORR catalytic activity in neutral media, which is comparable to commercial Pt/C (Figure 5D). The excellent ORR catalytic performance of Fe_{50}–N–C-900 SAEs over a wide range of pH is closely related to their morphological and compositional advantages. The porous structure with the large surface area can not only provide more exposed active sites but accelerate mass transport and electron transfer. Additionally, the homogeneous single active sites offer high catalytic efficiency.

In summary, Fe-doped MOF-derived Fe–N–C SAEs were successfully synthesized using a facile strategy. The single-atom features were confirmed by XRD, TEM, and X-ray adsorption techniques. By virtue of their high surface area

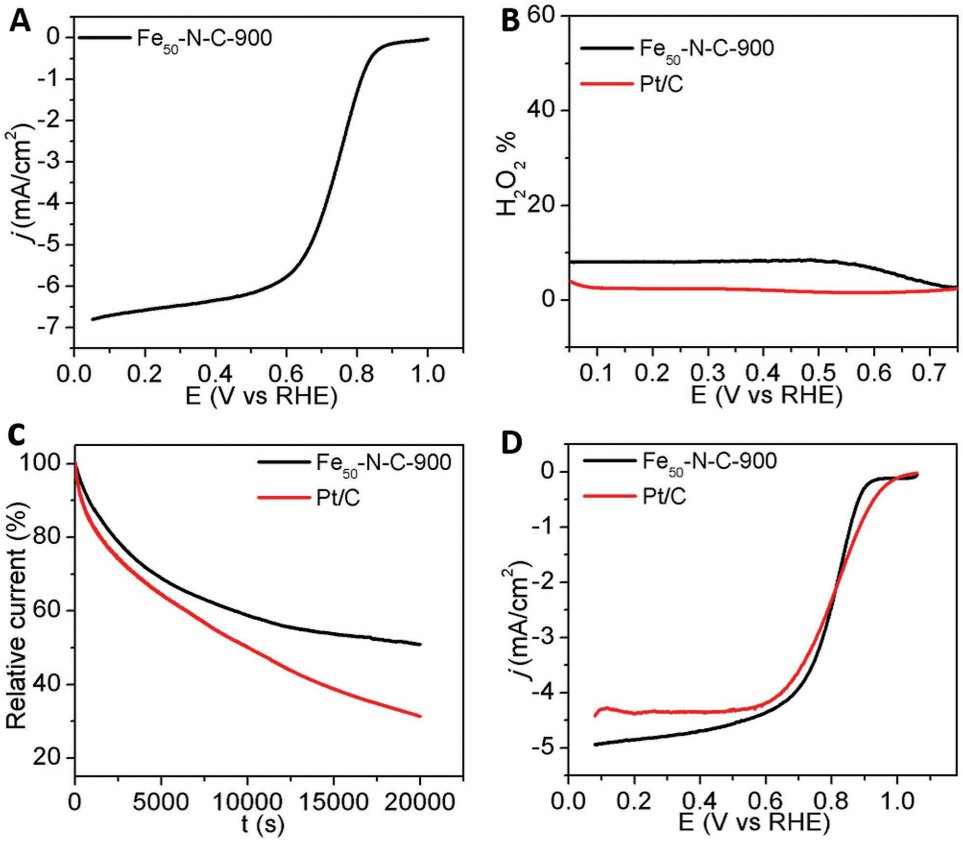

Figure 5. A) RDE polarization curves of Fe_{50}–N–C-900 (loading: 0.3 mg cm^{-2}) in O_2-saturated 0.1 M $HClO_4$ solution. B) The H_2O_2 yield percentage of Fe_{50}–N–C-900 and Pt/C derived from RRDE analysis. C) Long-term stability test of Fe_{50}–N–C-900 and Pt/C in O_2-saturated 0.1 M $HClO_4$ solution at 0.7 V with a rotation rate of 200 rpm. D) RDE polarization curves of Fe_{50}–N–C-900 (loading: 0.1 mg cm^{-2}) and Pt/C (loading: 0.1 mg cm^{-2}) in O_2-saturated 0.1 M PBS solution (pH = 7.4).

and homogeneous single active sites, the Fe–N–C SAEs with optimized synthesis condition possess superior ORR electrocatalytic activity in alkaline media. Remarkably, they present much better durability and methanol tolerance in comparison with the state-of-the-art Pt/C catalysts. Further electrochemical experiments demonstrate that Fe–N–C SAEs also possess excellent ORR catalytic performance in in acid and neutral media. Our work offers a new routine to prepare single-atom catalysts for ORR electrocatalysis.

Supporting Information

Supporting Information is available from the Wiley Online Library or from the author.

Acknowledgements

This work was supported by a start-up fund of Washington State University, USA. The XPS analysis was performed using EMSL, a national scientific user facility sponsored by the Department of Energy's Office of Biological and Environmental Research and located at Pacific Northwest National Laboratory (PNNL). The authors acknowledge Franceschi Microscopy and Image Center at Washington State University for TEM measurements. PNNL is a multiprogram national laboratory operated for DOE by Battelle under Contract DE-AC05-76RL01830.

Conflict of Interest

The authors declare no conflict of interest.

Keywords

Fe–N–C electrocatalysts, metal–organic frameworks, nonprecious metal nanocatalysts, oxygen reduction reaction, single-atom catalysts

Received: September 9, 2017
Revised: December 18, 2017
Published online:

[1] J. Liang, Y. Jiao, M. Jaroniec, S. Z. Qiao, *Angew. Chem., Int. Ed.* **2012**, *51*, 11496.
[2] C. Z. Zhu, H. Li, S. F. Fu, D. Du, Y. H. Lin, *Chem. Soc. Rev.* **2016**, *45*, 517.

[3] G. Q. Zhang, B. Y. Xia, C. Xiao, L. Yu, X. Wang, Y. Xie, X. W. Lou, *Angew. Chem., Int. Ed.* **2013**, *52*, 8643.
[4] K. N. Jung, J. Kim, Y. Yamauchi, M. S. Park, J. W. Lee, J. H. Kim, *J. Mater. Chem. A* **2016**, *4*, 14050.
[5] C. G. Hu, L. M. Dai, *Angew. Chem., Int. Ed.* **2016**, *55*, 11736.
[6] S. J. Guo, D. G. Li, H. Y. Zhu, S. Zhang, N. M. Markovic, V. R. Stamenkovic, S. H. Sun, *Angew. Chem., Int. Ed.* **2013**, *52*, 3465.
[7] Y. Z. Su, Z. Q. Yao, F. Zhang, H. Wang, Z. Mics, E. Canovas, M. Bonn, X. D. Zhuang, X. L. Feng, *Adv. Funct. Mater.* **2016**, *26*, 5893.
[8] C. Z. Zhu, S. J. Dong, *Nanoscale* **2013**, *5*, 1753.
[9] L. Wang, A. Ambrosi, M. Pumera, *Angew. Chem., Int. Ed.* **2013**, *52*, 13818.
[10] G. Wu, A. Santandreu, W. Kellogg, S. Gupta, O. Ogoke, H. G. Zhang, H. L. Wang, L. M. Dai, *Nano Energy* **2016**, *29*, 83.
[11] G. Wu, P. Zelenay, *Acc. Chem. Res.* **2013**, *46*, 1878.
[12] H. G. Zhang, H. Osgood, X. H. Xie, Y. Y. Shao, G. Wu, *Nano Energy* **2017**, *31*, 331.
[13] G. Wu, K. L. More, C. M. Johnston, P. Zelenay, *Science* **2011**, *332*, 443.
[14] M. Lefevre, E. Proietti, F. Jaouen, J. P. Dodelet, *Science* **2009**, *324*, 71.
[15] C. Z. Zhu, S. F. Fu, J. H. Song, Q. R. Shi, D. Su, M. H. Engelhard, X. L. Li, D. D. Xiao, D. S. Li, L. Estevez, D. Du, Y. H. Lin, *Small* **2017**, *13*, 1603407.
[16] S. R. Sun, N. Jiang, D. G. Xia, *J. Phys. Chem. C* **2011**, *115*, 9511.
[17] H. W. Liang, W. Wei, Z. S. Wu, X. L. Feng, K. Mullen, *J. Am. Chem. Soc.* **2013**, *135*, 16002.
[18] B. T. Qiao, A. Q. Wang, X. F. Yang, L. F. Allard, Z. Jiang, Y. T. Cui, J. Y. Liu, J. Li, T. Zhang, *Nat. Chem.* **2011**, *3*, 634.
[19] C. Zhu, S. Fu, Q. Shi, D. Du, Y. Lin, *Angew. Chem., Int. Ed.* **2017**, *56*, 13944.
[20] L. L. Lin, W. Zhou, R. Gao, S. Y. Yao, X. Zhang, W. Q. Xu, S. J. Zheng, Z. Jiang, Q. L. Yu, Y. W. Li, C. Shi, X. D. Wen, D. Ma, *Nature* **2017**, *544*, 80.
[21] N. C. Cheng, S. Stambula, D. Wang, M. N. Banis, J. Liu, A. Riese, B. W. Xiao, R. Y. Li, T. K. Sham, L. M. Liu, G. A. Botton, X. L. Sun, *Nat. Commun.* **2016**, *7*, 13638.
[22] P. Q. Yin, T. Yao, Y. Wu, L. R. Zheng, Y. Lin, W. Liu, H. X. Ju, J. F. Zhu, X. Hong, Z. X. Deng, G. Zhou, S. Q. Wei, Y. D. Li, *Angew. Chem., Int. Ed.* **2016**, *55*, 10800.
[23] Q. L. Zhu, W. Xia, L. R. Zheng, R. Q. Zou, Z. Liu, Q. Xu, *ACS Energy Lett.* **2017**, *2*, 504.
[24] H. J. Shen, E. Gracia-Espino, J. Y. Ma, H. D. Tang, X. Mamat, T. Wagberg, G. Z. Hu, S. J. Guo, *Nano Energy* **2017**, *35*, 8.
[25] Z. P. Zhang, X. G. Gao, M. L. Dou, J. Ji, F. Wang, *Small* **2017**, *13*, 1604290.
[26] B. W. Wang, X. X. Wang, J. X. Zou, Y. C. Yan, S. H. Xie, G. Z. Hu, Y. G. Li, A. G. Dong, *Nano Lett.* **2017**, *17*, 2003.
[27] S. F. Fu, C. Z. Zhu, J. H. Song, D. Du, Y. H. Lin, *Adv. Energy Mater.* **2017**, *7*, 1700363.
[28] H. Wang, Q. L. Zhu, R. Zou, Q. Xu, *Chem* **2017**, *2*, 52.
[29] B. Liu, H. Shioyama, T. Akita, Q. Xu, *J. Am. Chem. Soc.* **2008**, *130*, 5390.
[30] R. R. Salunkhe, C. Young, J. Tang, T. Takei, Y. Ide, N. Kobayashi, Y. Yamauchi, *Chem. Commun.* **2016**, *52*, 4764.
[31] R. R. Salunkhe, J. Tang, Y. Kamachi, T. Nakato, J. H. Kim, Y. Yamauchi, *ACS Nano* **2015**, *9*, 6288.
[32] M. Hu, J. Reboul, S. Furukawa, N. L. Torad, Q. Ji, P. Srinivasu, K. Ariga, S. Kitagawa, Y. Yamauchi, *J. Am. Chem. Soc.* **2012**, *134*, 2864.
[33] W. Chaikittisilp, N. L. Torad, C. L. Li, M. Imura, N. Suzuki, S. Ishihara, K. Ariga, Y. Yamauchi, *Chem. - Eur. J.* **2014**, *20*, 4217.
[34] B. You, N. Jiang, M. L. Sheng, W. S. Drisdell, J. Yano, Y. J. Sun, *ACS Catal.* **2015**, *5*, 7068.
[35] Y. Z. Chen, C. M. Wang, Z. Y. Wu, Y. J. Xiong, Q. Xu, S. H. Yu, H. L. Jiang, *Adv. Mater.* **2015**, *27*, 5010.
[36] X. J. Zhao, X. Q. Zou, X. C. Yan, C. L. Brown, Z. Q. Chen, G. S. Zhu, X. D. Yao, *Inorg. Chem. Front.* **2016**, *3*, 417.
[37] H. Y. Zhao, C. H. Sun, Z. Jin, D. W. Wang, X. C. Yan, Z. Q. Chen, G. S. Zhu, X. D. Yao, *J. Mater. Chem. A* **2015**, *3*, 11736.
[38] D. H. Lim, J. Wilcox, *J. Phys. Chem. C* **2012**, *116*, 3653.
[39] J. Liang, X. Du, C. Gibson, X. W. Du, S. Z. Qiao, *Adv. Mater.* **2013**, *25*, 6226.
[40] Y. Zhao, K. Watanabe, K. Hashimoto, *J. Am. Chem. Soc.* **2012**, *134*, 19528.
[41] L. F. Lai, J. R. Potts, D. Zhan, L. Wang, C. K. Poh, C. H. Tang, H. Gong, Z. X. Shen, L. Y. Jianyi, R. S. Ruoff, *Energy Environ. Sci.* **2012**, *5*, 7936.